

Global Biogeochemical Cycles®

RESEARCH ARTICLE

10.1029/2023GB007759

Key Points:

- Early spring peaks in N_2O flux from North American agriculture correlate to satellite soil freeze/thaw status from the previous winter
- A requisite frozen period in early winter appears necessary to prepare the soil for the freeze-thaw (FT) N_2O pulse
- Growing season N_2O emissions dominate FT emissions in U.S. agriculture but the two have comparable magnitude in Canada

Supporting Information:

Supporting Information may be found in the online version of this article.

Correspondence to:

C. Nevison,
Cynthia.Nevison@colorado.edu

Citation:

Nevison, C., Lan, X., & Ogle, S. M. (2023). Remote sensing soil freeze-thaw status and North American N_2O emissions from a regional inversion. *Global Biogeochemical Cycles*, 37, e2023GB007759. <https://doi.org/10.1029/2023GB007759>

Received 3 MAR 2023

Accepted 28 JUN 2023

Author Contributions:

Conceptualization: Stephen M. Ogle
Data curation: Xin Lan
Resources: Xin Lan
Writing – review & editing: Stephen M. Ogle

Remote Sensing Soil Freeze-Thaw Status and North American N_2O Emissions From a Regional Inversion

Cynthia Nevison¹ , Xin Lan^{2,3} , and Stephen M. Ogle⁴

¹University of Colorado/INSTAAR, Boulder, CO, USA, ²NOAA ESRL Global Monitoring Laboratory, Boulder, CO, USA,

³University of Colorado/Cooperative Institute for Research in Environmental Sciences (CIRES), Boulder, CO, USA, ⁴Natural Resource Ecology Laboratory, Colorado State University, Fort Collins, CO, USA

Abstract North American nitrous oxide (N_2O) emissions over 2011–2018 are estimated using the CarbonTracker-Lagrange regional inversion framework. Emissions are strongest in the Midwestern corn/soybean belt and display a distinct dual maxima seasonal pattern. The first maximum occurs in late winter/early spring, suggestive of freeze-thaw (FT) effects on denitrification rates and associated N_2O emissions. The second maximum occurs in late spring/early summer, consistent with a growing season nitrogen fertilizer-driven source, although fertilizer applied in late fall may contribute to the FT pulse as well. Interannual variability in the first maximum correlates significantly to soil freeze thaw status derived from remote sensing data. A requisite frozen period in the preceding early winter appears necessary to create conditions for the N_2O pulse after thawing. The FT pulse is a prominent feature of the annual cycle in Canadian cropland, where it may be of comparable magnitude to growing season emissions. In contrast, the growing season peak in N_2O dominates the FT peak in the Midwestern Corn-Soybean region of the United States.

1. Introduction

Nitrous oxide (N_2O) is both a long-lived greenhouse gas and ozone depleting substance whose atmospheric abundance is increasing at an accelerating rate (Lan et al., 2022; Liang et al., 2022; Ravishankara et al., 2009; Thompson et al., 2019). N_2O is produced through nitrification and denitrification in soils, freshwater and oceans by microbes that use nitrogen substrates, including synthetic N fertilizers, for their energetic metabolism. The anthropogenic N_2O source is growing in magnitude and now accounts for more than 40% of the total N_2O source (Canadell et al., 2021). Direct agricultural emissions are estimated to contribute more than half of the anthropogenic N_2O emissions. Substantial indirect agricultural emissions also occur due to the volatilization of other N-based gases, such as ammonia and nitrogen oxides, which are re-deposited on the earth's surface, and due to the leaching of organic N and nitrates into waterways (Canadell et al., 2021).

The countries participating in the UN Framework Convention on Climate Change estimate national emissions of N_2O from agricultural soils with a bottom-up methodology that assumes that such emissions occur mainly during the crop growing season (de Klein et al., 2006; Hergoualc'h et al., 2019; USEPA, 2021). However, recent literature has suggested that non-growing season emissions associated with winter freeze-thaw (FT) cycles in northern agricultural lands may be a substantial but previously overlooked source of anthropogenic N_2O that should be included in the IPCC methodology, which is used by countries for reporting to the UNFCCC (Del Grosso et al., 2022; Wagner-Riddle et al., 2017).

FT emissions are associated with bursts of microbial activity due to the readily available nitrogen and carbon in thawing soils and the anaerobic conditions occurring with the cycling between frozen and thawed phases in the late winter and early spring period. Wagner-Riddle et al. (2017) found that FT dynamics were a major control on the N_2O flux from agricultural land in Canada. They estimated, using a simple regression model, that the neglect of FT emissions potentially leads to an underestimation of global agricultural N_2O emissions of up to nearly 30%. Del Grosso et al. (2022) estimated, using a process-based model, that inclusion of FT dynamics increases annual N_2O emissions from croplands and grasslands by 11% nationwide in the U.S.

While the mechanisms are not fully understood, Congreves et al. (2018) present a conceptual diagram depicting how FT N_2O emissions might arise (see their Figure 2a). Such emissions typically occur as sporadic or transient pulses associated with changes in soil, for example, moisture or substrate availability, that are conducive to microbial denitrification. These sporadic pulses may be missed by bottom-up methods that are based on intermittent

soil sampling. In contrast, top-down regional atmospheric inversions of N_2O are particularly sensitive to large pulses, provided that atmospheric sampling frequency and spatial coverage are adequate to capture them (Nevison et al., 2018). Del Grosso et al. (2022) used results from the CarbonTracker-Lagrange (CT-L) regional inversion as supporting evidence for late winter/early spring FT N_2O pulses in the north central region of the United States. However, the inversion did not provide specific mechanistic evidence that the late winter/early spring peaks in N_2O are caused by FT dynamics.

In this paper, we compare remotely sensed FT status products from two satellites and correlate them to regional and interannual variability in winter/spring N_2O emissions from 2011 to 2018. We next derive a quantitative relationship to predict the interannual variability in the magnitude of N_2O FT emissions. Finally, we examine the relative importance of FT and growing season emissions from agricultural land across northern and more southerly latitudes in Canada and the United States.

2. Methods

2.1. Inversion Methodology

CT-L is a regional Bayesian inversion that begins with an objective “cost function” $\mathbf{J}(\mathbf{s})$ written as,

$$\mathbf{J}(\mathbf{s}) = \frac{1}{2} (\mathbf{z} - \mathbf{Hs})^T \mathbf{R}^{-1} (\mathbf{z} - \mathbf{Hs}) + \frac{1}{2} (\mathbf{s} - \mathbf{s}_p)^T \mathbf{Q}^{-1} (\mathbf{s} - \mathbf{s}_p), \quad (1)$$

The cost function is minimized and solved for optimized fluxes using algorithms described by Yadav and Michalak (2013).

$$\hat{\mathbf{s}} = \mathbf{s}_p + (\mathbf{HQ})^T (\mathbf{HQH}^T + \mathbf{R})^{-1} (\mathbf{z} - \mathbf{Hs}_p), \quad (2)$$

where, $\mathbf{s}_{(m \times 1)}$ is the surface flux in $\text{nmol m}^{-2} \text{s}^{-1}$. $\hat{\mathbf{s}}_{(m \times 1)}$ is the optimized surface flux in $\text{nmol m}^{-2} \text{s}^{-1}$. $\mathbf{s}_{p(m \times 1)}$ is the prior estimate of \mathbf{s} . $\mathbf{z}_{(n \times 1)}$ is a vector of N_2O observations, corrected by subtracting an empirical background value, in ppb. $\mathbf{H}_{(n \times m)}$ is a transport matrix, in ppb/($\text{nmol m}^{-2} \text{s}^{-1}$) that describes the relationship between the surface fluxes \mathbf{s} and the observations \mathbf{z} . $\mathbf{R}_{(n \times n)}$ is the model-data mismatch error covariance matrix, in ppb². $\mathbf{Q}_{(m \times m)}$ is the prior flux covariance error matrix in ($\text{nmol m}^{-2} \text{s}^{-1}$)², which is computed from a prescribed prior flux error vector σ_s in $\text{nmol m}^{-2} \text{s}^{-1}$, temporal correlation length in days and spatial correlation length in km.

The dimensions of the equation are defined as follows: m is the number of surface fluxes solved for in both time and space. n is the number of atmospheric observations.

The model configuration used here is similar to that described in detail in Nevison et al. (2018). Briefly, the prior was adapted from the year 2000 posterior flux of the global atmospheric N_2O inversion of Saikawa et al. (2014). Spatial and temporal correlation lengths of 300 km and 35 days, respectively, were used in \mathbf{Q} . Two alternative sets of parameters for σ_s and \mathbf{R} were used to represent alternative scenarios of more constrained prior/relaxed model-data mismatch (Case 1) and more relaxed prior/constrained model-data mismatch (Case 2). The square root σ_r of the main diagonal components of \mathbf{R} was 0.84 and 0.75 for Cases 1 and 2, respectively.

The \mathbf{H} matrices used in this study were constructed with footprints from two alternative particle dispersion models: (a) the Stochastic Time-Inverted Lagrangian Transport (STILT) model (Lin et al., 2003), which was driven by a Weather Research and Forecasting model (WRF) simulation customized for Lagrangian modeling (Nehrkorn et al., 2010) and (b) the Hybrid Single-Particle Lagrangian Integrated Trajectory (HYSPLIT) (Draxler & Hess, 1998; Stein et al., 2015) driven by the North American Mesoscale Forecast System (NAM) model, which has \sim 12 km resolution. NAM is the primary operational model used for mesoscale forecasting by the National Weather Service (NWS). The NAMS meteorological fields provided by NOAA's Air Resources Laboratory are archived in collaboration with the NWS, where the “S” in NAMS signifies that the meteorological fields are archived on the native “sigma” vertical levels of the model.

Atmospheric N_2O data used in the inversion were from the National Oceanic and Atmospheric Administration (NOAA) Global Greenhouse Gas Reference Network (<https://gml.noaa.gov/ccgg/about.html>). The NOAA GGRN includes \sim weekly paired flask samples (Lan et al., 2022) as well as tall towers (Andrews et al., 2014, 2022) and small aircraft (McKain et al., 2022; Sweeney et al., 2015) sites that use programmable

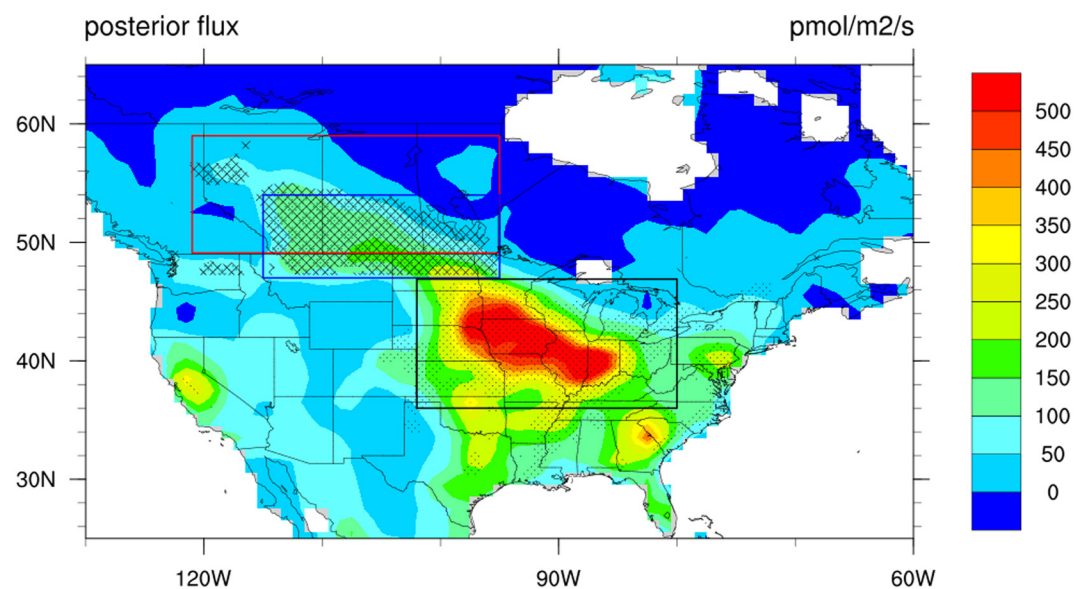


Figure 1. Mean posterior N_2O emissions averaged over Cases 1 and 2 and over 2011–2017 using National Oceanic and Atmospheric Administration N_2O data only and STILT-WRF footprints. Black, blue and red boxes show the geographic bounds of Midwestern Corn/Soybean, Northern Wheat, and Canadian Cropland respectively. These regions are narrowed further based on crop coverage, where dotted stippling shows areas in which more than 5% of land is planted in corn/soybean and wheat inside the Midwestern Corn/Soybean and Northern Wheat box, respectively, and cross hatched stippling shows areas in which more than 10% of the land is planted in crops of any kind in the two northern boxes.

12-flask sampling systems. At tower sites, air samples are mostly collected in mid-afternoon, with a typical sampling frequency between 1 and 3 days. At aircraft profiling sites, the sampling system units are collected at different altitudes from ~ 500 magl up to $\sim 8,000$ masl. All samples are shipped to the NOAA Global Monitoring Laboratory in Boulder, Colorado, USA, for analysis of N_2O on a gas chromatograph with electron capture detection, calibrated with a suite of standards on the WMO X2006A scale maintained by NOAA GML (Hall et al., 2007). Uncertainties of the measurements (68% confidence interval) for the period of this study range from 0.26 to 0.43 ppb. The data were filtered to exclude air samples collected 4,000 m or more above the local surface. These data generally had small surface influence footprints but were occasionally influenced by episodic stratospheric intrusions of highly N_2O -depleted air, which the inversion framework is not well equipped to handle.

The atmospheric N_2O observations were adjusted by subtracting an empirically determined background value to compute the vector \mathbf{z} . The background value was estimated based on the intersection of the back trajectories used to compute the footprints in \mathbf{H} with a four-dimensional time-varying field covering North America and its surrounding oceans. The inversion was run with a daily time step for each year from 1 January 2011 to 31 December 2018, the time frame corresponding to the overlapping availability of remote sensing-based freeze thaw data and HYSPLIT and STILT footprints. For computational reasons, this 8-year time span was divided into eight separate, partly overlapping inversions. To avoid end effects, these were centered around each calendar year but padded by the previous December and the following January (except for the 2018 STILT footprints, which extend only through 31 May).

2.2. Agricultural Data Sets

The area of cropland was based on the agricultural data set described in Levis et al. (2012), which was adapted from earlier work by Ramankutty and Foley (1998) and is in units of percentage of total grid area planted in major crop types, including corn, soybean and wheat, on a $0.5^\circ \times 0.5^\circ$ global grid. Since the land area used for corn and soybean substantially overlaps, these were consolidated into a single category designated as corn/soybean. The crop area data set was used to identify three North American regions of special interest (Figure 1). Two of these

regions were delineated based on mutually exclusive latitude/longitude bounds, with the additional requirement of a minimum grid cell coverage of 5% corn/soybean or wheat, respectively:

Midwestern Corn/Soybean: 36°N to 47°N, 102°W to 80°W, >5% coverage of corn/soybean in the U.S.;

Northern Wheat: 47°N to 54°N, 115°W to 95°W, >5% coverage of wheat, spanning the U.S. and Canada.

An additional region, Canadian Cropland, was defined. This largely overlaps with Northern Wheat but includes all crops and is centered farther to the north, entirely in Canada.

Canadian Cropland: >49°N, >95°W, >10% coverage of all crops combined.

Statewide crop progress data were used as a proxy for the timing of synthetic N fertilizer application, which generally occurs around the time of planting (Lu et al., 2022; Nishina et al., 2017). Crop progress data record the weekly percentage of a given crop planted within a given state and were obtained from the USDA Quick_Stats Lite database (www.nass.usda.gov). These data were used to distinguish the post-fertilization N₂O emissions maximum from the pre-fertilization, presumed FT peak. For Midwest Corn/Soybean, corn data from Iowa were used because Iowa lies in the heart of the region and corn is fertilized at much higher rate than soybean (a leguminous N₂ fixing crop). For Northern Wheat, wheat crop progress data from North Dakota were used.

For each integrated region, we computed a regionally aggregated posterior flux covariance matrix to estimate the random uncertainty in the aggregated fluxes. The posterior flux covariance matrix was computed monthly as a function of **Q**, **H**, and **R** (e.g., Yadav & Michalak, 2013) and was extrapolated daily by linearly interpolating between months. In addition to individual annual seasonal cycles, the mean seasonal cycle over 2011–2017 ($N = 7$ years) was computed and the corresponding mean posterior flux uncertainty was estimated as the inverse square root of $1/N$ times the sum of the inverse square root of the uncertainties for each year. This mean uncertainty was designed to represent the typical uncertainty in any given year with the assumption that there was no reduction in uncertainty achieved by averaging over the 7-year span. (Note: the multi-year mean excluded 2018 due to the incomplete coverage of STILT footprints for that year).

2.3. Remote Sensing Soil Freeze/Thaw (FT) Status

Three different satellite products reflecting soil FT status in North American soil were compared as daily integrals over the three crop regions described above.

The first two products were from the polar orbiting Soil Moisture Active-Passive (SMAP) mission (<https://smap.jpl.nasa.gov/>) accessed at <https://search.earthdata.nasa.gov/>. The SMAP mission primarily uses passive (radiometer) L-band microwave remote sensing to determine the land surface soil moisture and FT state. SMAP was launched in November 2014. Operational data became available starting 31 March 2015 and continue through the present, thus overlapping with CT-L results through December 2018. SMAP Enhanced L3 Radiometer Global and Northern Hemisphere Daily 9 km EASE-Grid FT State V003 consists of a daily composite of landscape FT state for the boreal land region north of 45°N latitude. SMAP L4 Global Daily 9 km EASE-Grid Carbon Net Ecosystem Exchange V006 FT data were also analyzed. This second data set is a model-derived value-added product provided as part of the carbon net ecosystem exchange package that supports key SMAP applications.

Additional FT status data were obtained from the European Space Agency's Soil Moisture and Ocean Salinity (SMOS) mission. SMOS is a sun-synchronous, polar orbiting satellite. The SMOS Level 3 Freeze and Thaw product, available at <https://smos-diss.eo.esa.int/oads/access/>, provides daily information on the soil state in the Northern Hemisphere based on SMOS observations. SMOS was launched on 2 November 2009, with the first FT data available from July 2010. The SMOS data overlap with the CT-L inversion for nearly a decade from December 2010–December 2018. SMOS data are reported daily on an irregular grid, nominally at 25 km resolution. Unlike SMAP, which reports only two possible soil states: thawed and frozen, SMOS has a third “partial” category. As a default assumption “partial” was assigned as 50% frozen, but alternative assumptions of 25% and 75% were also tested. The results of these assumptions as well as the differences between SMOS L3 and SMAP L3 and L4 are discussed below.

The daily percentage of frozen soil in each of the three agricultural regions described above was defined by (a) averaging the frozen fraction of all satellite pixels in each $1^\circ \times 1^\circ$ grid in the CT-L domain and multiplying by the grid area, (b) integrating these fractional frozen areas over all grids in each agricultural region, (c) dividing by the total area of the region and multiplying by 100. In addition, the cumulative frozen days (CFD) total in each region was computed by integrating the daily frozen percentages each day over a specified time interval. The CFD was also calculated at the $1^\circ \times 1^\circ$ grid level, as shown in Figure 2.

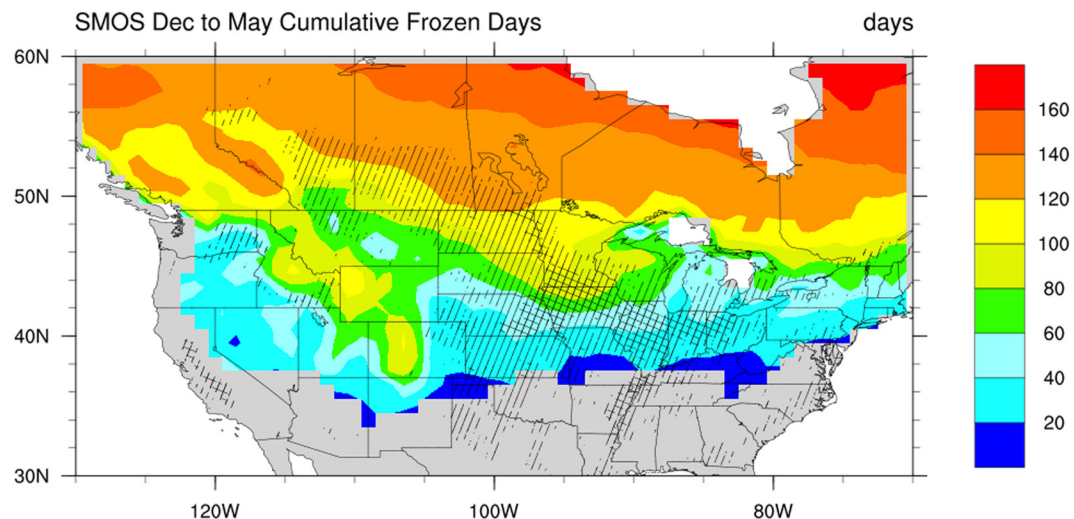


Figure 2. Soil cumulative frozen days from 1 December to 31 May (182 days total) from SMOS averaged over the winter seasons of 2011–2012 to 2017–2018. Stippling shows areas receiving synthetic N fertilizer input at a rate (divided over the total grid area) of at least 10 kg N/ha/yr (single diagonal lines) or at least 50 kg N/ha/yr (cross hatched lines) based on the Sustainability and the Global Environment (SAGE) data set (www.sage.uwisc.edu) (Nevison et al., 2018). FT N₂O pulses are most likely in regions that experience winter freezing and that may also contain excess soil nitrate due to regular N fertilizer input.

Surface soil temperature data were obtained from the North American Regional Reanalysis (NARR). These data are provided at 3-hourly mean resolution on the NARR 32 km Lambert grid (Mesinger et al., 2006; NCEP, 2005), which were averaged daily and within each CT-L grid and integrated over the regions of interest in the same manner described above for the FT data.

3. Results

The three remote sensing FT products show distinct features but follow a generally similar temporal course of soil thawing in the Midwestern Corn/Soybean belt. On a given day, SMAP L4 predicts a substantially larger area of frozen soil than SMAP L3, with SMOS L3 falling in between the two SMAP datasets (Figure 3). Alternative assumptions of 25%, 50%, or 75% frozen for the SMOS FT “partial” category yield similar results, when integrated over Midwestern Corn/Soybean (Figure 3b). NARR soil temperature data independently corroborate that the soil has warmed above freezing around the time that the satellite FT products show near-complete thawing of soil (Figure 3c).

Figure 3 focuses on 2017 due to a large probable freeze thaw emission pulse in mid to late February of that year. Two exceptionally high excursions from background in atmospheric N₂O of 12 and 22 ppb were observed in NOAA data at West Branch, Iowa. In addition, excursions of 11 ppb or higher were observed over Iowa in four low altitude flask samples collected by the ACT-America aircraft campaign (Davis et al., 2018; Eckl et al., 2021; Wei et al., 2021). The corresponding STILT-WRF influence footprints extended across Iowa and parts of Nebraska, South Dakota, and Wisconsin (Figure S1 in Supporting Information S1), leading to a large late-February emission pulse in the inversion results across much of the Midwest (Figure 3). All FT products show a near complete thawing of Midwestern soil during the third week of February 2017, coincident with the N₂O pulse (Figure 3). Notably, the 2017 thaw occurred unusually early compared to other years in the decade (Figure 4).

The Midwestern Corn/Soybean belt, the hotspot of N₂O emissions for North America, shows a distinct dual maxima seasonal pattern (Figures 1 and 4). The second maximum invariably begins its rise around or slightly after the time of corn planting, which serves as a proxy for the approximate time of nitrogen fertilizer application. In contrast, the early peak occurs well before the time of corn planting, generally between mid-February and mid-April. It also displays more interannual variability, both with respect to timing and magnitude, and is generally shorter in duration than the later growing season peak. In some years, the early peak is hardly discernible, while in other years, it is comparable or even larger than the growing season peak.

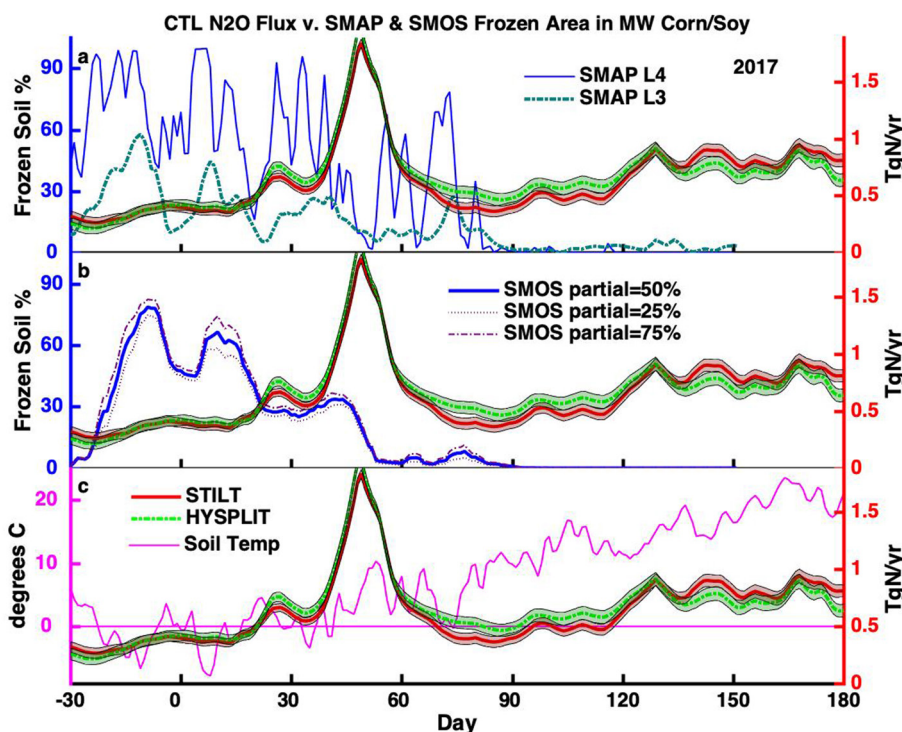


Figure 3. Posterior N₂O flux integrated over Midwest Corn/Soybean in 2017, which had an exceptionally strong FT N₂O pulse during February. Results using the STILT-WRF and HYSPLIT-NAMS particle dispersion models are shown in red and green, respectively, with Case 1 covariance parameters for both models. The top panel compares Soil Moisture Active-Passive L3 and L4 soil FT status, shown as the area of frozen soil integrated over the Corn/Soybean Belt as a percentage of the total area. The middle panel shows SMOS L3 FT, comparing the sensitivity of assuming 25%, 50%, and 75% frozen soil when freeze thaw status is reported as “partial.” The bottom panel compares North American Regional Reanalysis soil temperature. Note that the X axis extends from the previous December 1 (day -30) of 2016 through the end of June 2017.

The relationship between the early N₂O flux peak and soil FT status was explored by plotting the cumulative N₂O emissions from 15 February to 15 April against cumulative frozen days (CFD) of soil over the previous 1 December–31 January. CFD was found to be correlated significantly ($p < 0.001$) to the subsequent cumulative N₂O emission in late winter/early spring (i.e., the 2 months encompassing the approximate period after soil thaw but prior to synthetic N fertilizer application) (Figure 5). Similar correlations were found when the N₂O integral was extended to late April or the CFD period was extended into mid-February, but the correlation weakened substantially ($p = 0.09$) when the previous December was omitted from the CFD integral (Figure S2 in Supporting Information S1). The correlation also weakened ($p = 0.07$) when the N₂O integral was extended to encompass the full winter/early spring period from 1 December to 15 April (Figure S3 in Supporting Information S1).

The Northern Wheat and Canadian Cropland regions also show hints of the same dual maxima seasonal pattern in N₂O flux, although these northern regions are less well resolved by the inversion and have substantially higher posterior flux uncertainty than Midwest Corn/Soybean. In Northern Wheat (Figure S4 in Supporting Information S1), the second N₂O flux peak generally begins to rise after the time of spring wheat planting, while the early peak occurs before spring wheat planting. The early peak appears to coincide with soil thawing in some years (e.g., 2012 and other even years). However, in some odd years (2011, 2013 and, for the HYSPLIT configuration, 2017) the early peak occurs when soil in the Northern Wheat region is still nearly 100% frozen. Notably, the exceptionally large February 2017 FT peak seen in Midwest Corn/Soybean is barely discernible in Northern Wheat in the STILT configuration and is relatively small even in the HYSPLIT configuration.

The climatological mean seasonal cycle in N₂O emissions across all three regional integrals (Midwest Corn/Soybean, Northern Wheat, Canadian Cropland) shows an N₂O flux maximum that coincides with the onset of soil thawing. In Midwestern Corn/Soybean, the large FT N₂O pulse in February 2017 shifts the range of the climatological mean FT pulse to a broad low peak spanning February and March (Figure 6). The 2017 excursion has relatively less impact on the more northerly regions, where the pulse remains centered around late March.

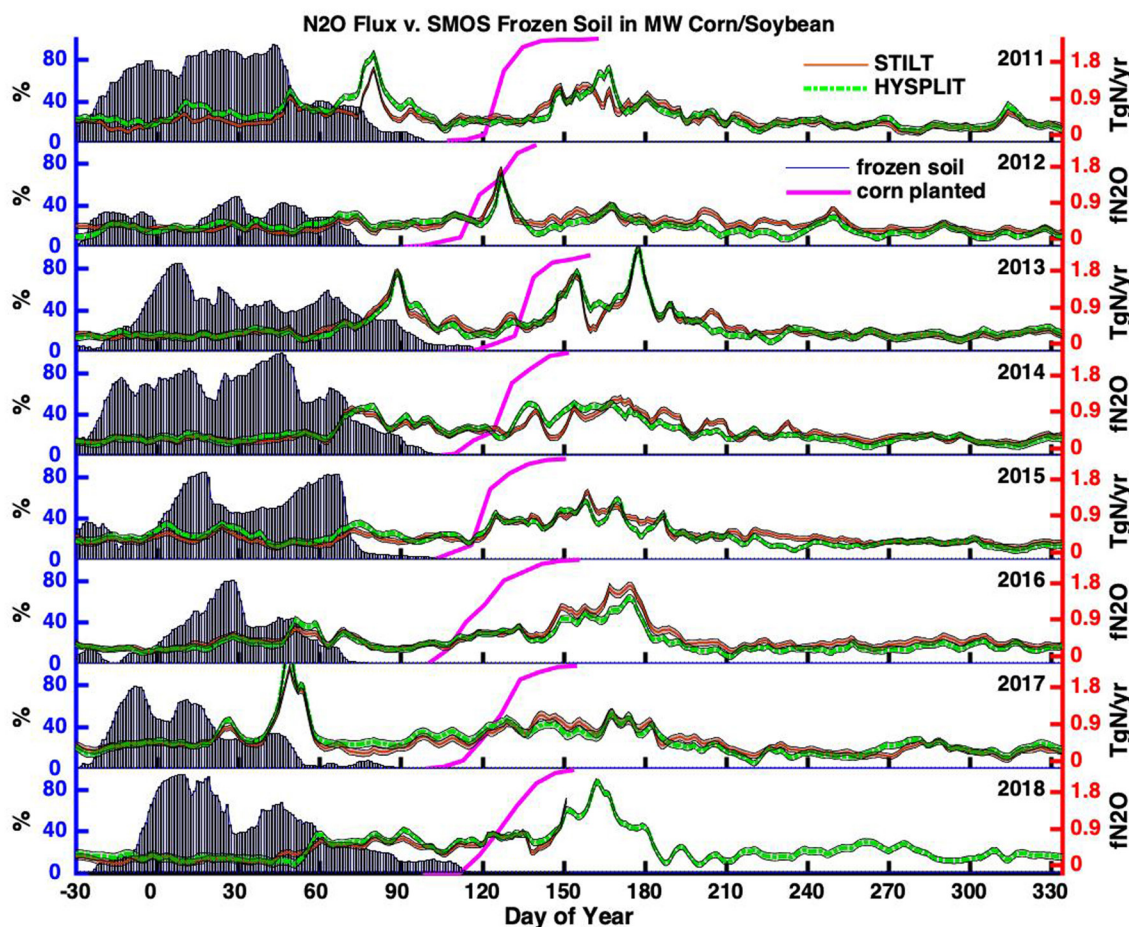


Figure 4. Posterior N_2O flux integrated over Midwestern Corn/Soybean from 2011 to 2018. Results using the STILT-WRF and HYSPLIT-NAMS particle dispersion models are shown in red and green, respectively, with Case 2 covariance parameters for both models. The percentage area of frozen soil is shown in blue bars for the SMOS satellite, integrated over Midwestern Corn/Soybean. Also shown is the percentage of corn planted in Iowa from USDA crop progress data. Note that the X axis extends from the previous December 1 (day -30) to November of the current year.

The relative magnitude of the FT N_2O maximum compared to the later fertilizer/growing season maximum also decreases along the north to south gradient (Figure 6). In Midwestern Corn/Soybean, the FT maximum is clearly dominated by the growing season maximum, but the two maxima are more comparable in magnitude for the Northern Wheat region. In Canadian Cropland, the FT maximum tends to exceed the growing season maximum, at least for the Case 2 parameters.

4. Discussion

In the agricultural regions of the central U.S. and Canada, the N_2O annual cycle has two distinct maxima, which vary interannually but are readily distinguishable in the multi-year mean. The second maximum appears closely related to crop planting dates and synthetic N fertilizer application. The early N_2O peak, which appears related to soil FT dynamics, is the focus of this paper.

Pulses of N_2O emissions are well known to occur during freeze thaw cycles as the season changes from winter to spring based on field studies and soil modeling (Del Grosso et al., 2022; Tenuta et al., 2019; Wagner-Riddle et al., 2017). The current study provides additional top-down evidence for the phenomenon. First, the timing of the FT N_2O peak predicted by the inversion, typically between day 70–90 in the Midwest Corn/Soybean belt (with the exception of the early peak in 2017 around day 50), is consistent with flux data measured at a long-term experimental cropland site at a similar latitude (43.7°N) located in Ontario (Wagner-Riddle et al., 2017). Second, the observed early N_2O peak in the Midwest Corn/Soybean belt shifts year to year depending on the timing of thawing. Third, the magnitude of the peak varies depending on the cumulative period of frozen soil earlier in the winter. The

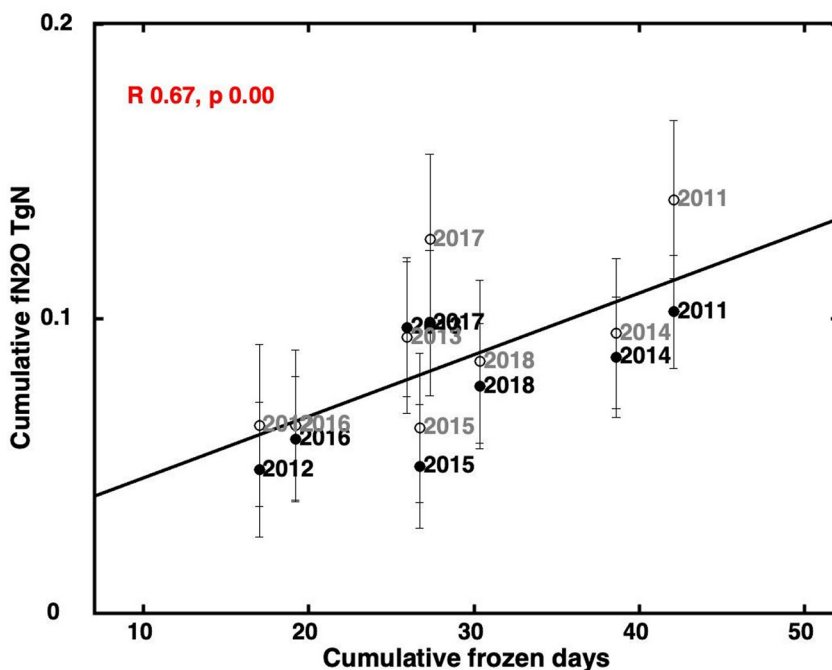


Figure 5. Posterior N₂O flux by year from 15 February to 15 April versus soil cumulative frozen days from SMOS L3 FT from the previous 1 December–31 January. N₂O flux and percent frozen soil are integrated daily over Midwestern Corn/Soybean. Both Stochastic Time-Inverted Lagrangian Transport and HYSPLIT N₂O fluxes are included and shown as filled and open circles with black and gray labels, respectively.

extent of freezing from December to January appears particularly important for the magnitude of the FT peak. In years without substantial early winter freezing, the FT N₂O peak is not easy to discern or is even absent from the seasonal pattern. Conversely, the peak is most prominent in years with more widespread freezing in early winter. This relationship can be inferred by visual inspection (Figure 4) and is supported by the significant correlation between late winter/early spring N₂O emissions and the CFD from the preceding winter months (Figure 5).

The correlation is consistent with the theory that agricultural soil needs to undergo a period of freezing for the N₂O pulse to occur in late winter/early spring (Congreves et al., 2018; Del Grosso et al., 2022; King et al., 2021). The frozen period creates selective pressure that favors microbes capable of efficient denitrification and permits the accumulation of soluble C in soil from microbial death during the frozen period (King et al., 2021). Upon thawing of soil, this C fuels high rates of microbial denitrification with associated N₂O emission. In the case of a warm late fall and winter, the lack of freezing decreases the amount of soluble C substrate that becomes available, preventing high rates of denitrification during spring thaw (King et al., 2021). This leads to relatively low rates of N₂O emissions that are not detected as a pulse based on the atmospheric observations and the inversion analysis. Notably, there is no discernible difference in the N₂O emissions in warmer versus cooler Decembers; the fluxes are low in either case, suggesting that the pulse is not displaced to the fall or early winter with warmer conditions (Figure 4). This result is consistent with laboratory soil core incubations showing that a longer period of freezing is needed to activate the mechanisms leading to FT pulses (King et al., 2021). However, the weakening of the N₂O flux versus CFD correlation when N₂O emissions are summed over 1 December–15 April rather than just 15 February–15 April suggests that some compensating early winter N₂O emissions in years without a discernible FT pulse cannot be ruled out given the uncertainties of the inversion.

The cumulative emission of N₂O over the whole late fall to early spring period ranges from about 0.11 to 0.24 Tg in years with a discernible FT pulse and on the order of 0.1 Tg N in years without a discernible pulse (Figure S3 in Supporting Information S1). Dividing by the area ($\sim 1,300 \times 10^5$ ha) of the Midwestern Corn/Soybean belt, as defined in Section 2.2, yields a typical cold season N₂O flux of 0.8–1.8 kg N/ha. This is consistent, within the large uncertainties, of the cumulative cold season (November–April) release of 0.2–2.3 kg N₂O-N/ha estimated by Wagner-Riddle et al. (2017) based on observed N₂O fluxes from agricultural land in Michigan. In addition, a comparison to site specific observations at Glenlea, Manitoba (Tenuta et al., 2019) suggests that the inversion is

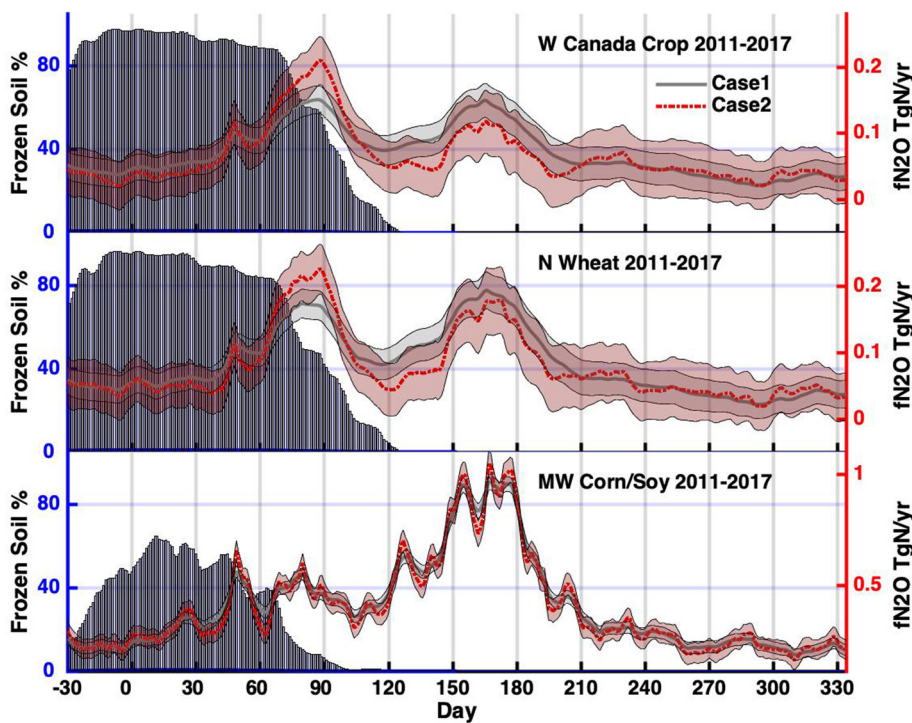


Figure 6. Mean annual cycle in the posterior N_2O flux averaged over 2011–2017 and integrated over Canadian Cropland, Northern Wheat, and Midwestern Corn/Soybean. Cases 1 and 2 results are shown in gray and red, respectively, with the STILT-WRF particle dispersion model used for both cases. The percentage of frozen soil from SMOS, integrated over each respective region and averaged over 2011–2017, is shown in blue bars. Note that the bottom panel has an expanded Y axis scale compared to the upper panels and that the X axis extends from the previous December 1 (day –30) to November of the current year in all panels.

capturing the timing and magnitude of the observed FT and growing season fluxes reasonably well, within the large margin of uncertainty (Figure S5 in Supporting Information S1).

Although the FT emissions occur before the current year's planting of crops, ultimately, the substrate for the N_2O pulse is influenced by fertilizer, which is added to the previous year's crop and may still be present as residual soil inorganic N (Glenn et al., 2012; Wagner-Riddle et al., 2017). This may be especially true for spring FT emissions in years when soil N loss during the previous year's growing season is relatively low. For example, in the drought year 2012, nitrate loss to the Gulf of Mexico, via the Mississippi River which drains the Midwestern soybean belt, was a factor of 2–3 times lower than in surrounding years (NCCOS, 2022). Denitrification loss of soil nitrate was also likely substantially reduced in 2012, as evidenced by the abnormally low growing season N_2O flux (Figure 4) (Nevison et al., 2018). If extra residual soil N remained after the 2012 growing season, it may have contributed to the strong FT peak in spring 2013, despite the only modest CFD value for the previous winter (Figure 5).

Another consideration is that fall fertilizer application, a common practice in the U.S. Midwest corn/soybean belt (Nowatzke & Arbuckle, 2016), may provide additional inorganic N substrate for the FT pulse. Fall fertilization typically involves injecting anhydrous ammonia 30–45 cm deep in the soil after temperatures have cooled below $\sim 10^\circ\text{C}$, typically in October/November after harvest, with a nitrification inhibitor added to prevent conversion to nitrate. Both of those factors tend to suppress microbial metabolism of the applied fertilizer, which may explain why the inversion does not show a discernible uptick in N_2O fluxes in late fall (Figures 4 and 6). Consistent with the above discussion, field observations in Manitoba suggest that late-fall fertilizer application does not trigger immediate emissions of N_2O but does lead to an increased FT pulse of N_2O during the subsequent year's thaw (Tenuta et al., 2016).

4.1. Implications for Global N_2O Inventories

While much of the field-based evidence for the FT peak comes from croplands in Canada (Tenuta et al., 2019; Wagner-Riddle et al., 2017), some global emission inventories, for example, EDGAR v 4.3.2, prescribe a

universal March maximum in N_2O emissions (see discussion below) with relatively low emissions in summer (EDGAR4.3.2., 2017). Other inventories, for example, EDGAR 5.0 and GEIA, do not resolve seasonality and provide only a mean annual value of agricultural N_2O emissions (EDGAR5.0., 2019; Miller et al., 2012). Either approach has led to confusion when inventory fluxes are used to force atmospheric transport models for comparison to atmospheric N_2O data measured by aircraft campaigns over the U.S. Midwest. These campaigns typically are confined to a restricted time frame, for example, 1–2 months, often in summer. Thus, if the aircraft campaigns coincide with the peak enhancements in atmospheric N_2O in May or June, they may infer large fluxes and conclude that the inventories significantly underestimate N_2O emissions and/or have inappropriate seasonality (Eckl et al., 2021; Kort et al., 2008; Miller et al., 2012).

Interestingly, the EDGAR 4.3.2 March peak appears to be based not on FT emissions measured in northern regions and extrapolated globally but rather on agricultural modeling of ammonia emissions with seasonality extrapolated to N_2O (Asman, 1992; Janssens-Maenhout et al., 2019). Regardless, the results presented here add to the evidence that March is generally not the appropriate month for the primary N_2O maximum in the U.S. Midwest Corn/Soybean belt, which is the largest source region of N_2O in North America.

In the Midwestern Corn/Soybean belt, by far the highest emissions are in the post fertilization period from May to July. In the Northern Wheat and Canadian Cropland regions, the FT peak appears relatively more important and is similar in magnitude to the growing season N_2O peak. That said, there is similarity of the seasonal timing across the North-South gradient (Figure 6). This, when combined with the stronger signal-to-noise ratio of the N_2O data in the U.S. Midwest than in other regions, suggests that N_2O monitoring sites in the U.S. Midwest, with 10-day back trajectory footprints extending northwest into Canada, may in part drive the seasonal cycle across all latitudes. In particular, the FT peak occurs in March for 2011 and 2013 based on the inversion in Northern Wheat region, when soil in that region is still 80% or more frozen (Figure S4 in Supporting Information S1). It is also notable that site-level measurements at a long-term agricultural research site in Manitoba, Canada show larger peak N_2O fluxes in response to spring fertilizer application than to FT events (Figure S5 in Supporting Information S1) (Tenuta et al., 2019).

4.2. Uncertainties and Differences Among Satellite Freeze Thaw Products

Differences in satellite FT products also create uncertainty in our analysis. While the three FT products examined here follow similar patterns year to year, they also display distinct differences. For example, SMAP L4 predicts larger areas of frozen soil than SMAP L3 and is characterized by more frequent oscillations between frozen and thawed conditions. This may reflect the fact that L4 is an assimilated model product that is sensitive to air temperature, which may be more prone to fluctuation than soil-based temperature metrics (Xiaolan Xu, personal communication). Given the discrepancies between SMAP L3 and L4, combined with the fact that SMOS data are available for a longer period of time, that is, from late 2010 onward (whereas SMAP data are only available from April 2015 onward), we focused on SMOS in our comparison of FT data to the inversion results. Another consideration was that SMAP FT data are optimally designed for latitudes north of 45°N, whereas the Midwest Corn/Soybean belt lies mostly south of that latitude. Notably, in the Northern Wheat region, which is entirely north of 45°N, SMOS, SMAP L3 and L4, FT have similar relative patterns, with SMOS mainly falling between SMAP L3 and L4 (Figure S6 in Supporting Information S1). Finally, the SMOS transition from frozen to thawed soil was generally consistent with the rise in soil temperatures above 0°C seen in NARR, which provided an independent check on soil thaw status (Figure 3).

A separate source of uncertainty is the difference in spatial scales between the satellite data, available at 9 and 25 km resolution for SMAP and SMOS, respectively, and the posterior inversion results, which assume a 300 km correlation length scale. For this reason, our analysis focused on large regional integrals rather than trying to correlate at the scale of individual satellite pixels. The inversion results themselves are variable depending on parameter assumptions and choice of particle dispersion model. In Midwest Corn/Soybean belt, the posterior fluxes were generally consistent between Cases 1 and 2 and between NAMS-HYSPLIT and STILT-WRF, but the differences were larger and the uncertainties greater in Northern Wheat and Canadian Cropland regions.

The sensitivity of the inversion was tested to a range of prescribed correlation length parameters in the prior flux covariance uncertainty matrix \mathbf{Q} (Yadav & Michalak, 2013). The temporal correlation length was set alternatively at 7 and 14 days, in addition to the standard value of 35 days, and the spatial correlation length was set alternatively

at 100 and 500 km, in addition to the standard value of 300 km, based on the ranges used in applications of CT-L for other long-lived natural greenhouse gases (Hu et al., 2019). These choices led to nine different permutations of \mathbf{Q} for each simulation year. The variance in the posterior results, as quantified by the standard deviation in the regionally integrated fluxes among the nine permutations, was used to define the parametric uncertainty.

In addition, the random uncertainty due to factors such as transport error, measurement error, the sparsity of the observation network, etc. for each simulation and region of interest was estimated by computing a regionally aggregated posterior flux covariance matrix. This matrix is a function of \mathbf{H} , \mathbf{Q} , and \mathbf{R} and reflects the influences of the available influence footprints (represented by \mathbf{H}) as they intersect with the prescribed \mathbf{Q} and \mathbf{R} covariance matrices (Yadav & Michalak, 2013).

The sensitivity tests reveal that the random uncertainty dominates the parametric uncertainty in Northern Wheat and Canadian Cropland. In contrast, the parametric uncertainty dominates the random uncertainty in Midwestern Corn/Soybean, especially during extreme events such as the February 2017 FT pulse (Figure S7 in Supporting Information S1). These disparate results are consistent with the naturally large posterior flux covariance in regions that are not well represented in \mathbf{H} . In contrast, in regions that are well represented by influence footprints in \mathbf{H} , such as Midwestern Corn/Soybean, the assumed correlation length scales over which signals in the atmospheric data are extrapolated in time and space are the major uncertainty in the posterior fluxes.

5. Conclusions

N_2O emissions from North American agriculture display two distinct maxima, one in late winter/early spring and the second in late spring early summer. The second maximum appears closely related to synthetic N fertilizer application during the crop growing season, while the first appears related to soil FT dynamics. This study demonstrates for the first time a discernible relationship between remote sensing soil FT status and top-down estimates of N_2O fluxes from an atmospheric inversion. Despite some discrepancies in satellite soil FT products, the cumulative frozen soil days across the previous December and January are correlated to the magnitude of subsequent late winter/early spring N_2O emissions. A requisite frozen period appears to be needed to create conditions favorable for the microbial-driven N_2O pulse during FT cycles. Global emissions inventories would more accurately capture the seasonality of North American N_2O emissions with a May/June primary maximum and a smaller secondary maximum in late winter that increases in importance along a south to north gradient in agricultural regions.

Data Availability Statement

The data used in this study can be obtained through the NOAA Global Monitoring Laboratory at https://gml.noaa.gov/ftp/data/trace_gases/n2o/ (Lan et al., 2022) or by contacting xin.lan@noaa.gov. The CarbonTracker-Lagrange inversion code is described at www.esrl.noaa.gov/gmd/ccgg/carbontracker-lagrange/doc/ (Thoning et al., 2019).

Acknowledgments

CDN and SO acknowledge support from NASA award 80NSSC20K1804. We thank Steve DelGrosso, Lei Hu and two anonymous reviewers for their helpful comments on the results presented here. We are grateful to Arlyn Andrews and Kirk Thoning for developing and providing guidance on the inversion framework and to Thomas Nehrkorn and Marikate Mountain for providing WRF-STILT footprints. We thank Ed Dlugokencky and the many other people who have contributed to the production of the excellent N_2O datasets that made this study possible. Finally, we thank Mario Tenuta for providing N_2O data from the Trace Gas Manitoba (TGA-MAN) Long-term Crop Flux Study.

References

- Andrews, A. E., Crotwell, A., Crotwell, M., Handley, P., Higgs, J., Kofler, J., et al. (2022). NOAA global greenhouse gas reference network flask-air PFP sample measurements of N_2O at tall tower and other continental sites, 2005-present, version: 2022-11-01. <https://doi.org/10.15138/C11N-KD82>
- Andrews, A. E., Kofler, J. D., Trudeau, M. E., Williams, J. C., Neff, D. H., Masarie, K. A., et al. (2014). CO_2 , CO , and CH_4 measurements from tall towers in the NOAA Earth system research Laboratory's global greenhouse gas reference network: Instrumentation, uncertainty analysis, and recommendations for future high-accuracy greenhouse gas monitoring efforts. *Atmospheric Measurement Techniques*, 7(2), 647–687. <https://doi.org/10.5194/amt-7-647-2014>
- Asman, W. A. H. (1992). *Ammonia emission in Europe: Updated emission and emission variations*, rep. 228471008. National Institute for Public Health and Environment Protection.
- Canadell, J. G., Monteiro, P. M. S., Costa, M. H., Cotrim da Cunha, L., Cox, P. M., Eliseev, A. V., et al. (2021). Global carbon and other biogeochemical cycles and feedbacks. In V. Masson-Delmotte, P. Zhai, A. Pirani, S. L. Connors, C. Péan, S. Berger, et al. (Eds.), *Climate change 2021: The physical science basis. Contribution of working group I to the sixth assessment report of the intergovernmental panel on climate change* (pp. 673–816). Cambridge University Press. <https://doi.org/10.1017/9781009157896.007>
- Congreves, K. A., Wagner-Riddle, C., Si, B. C., & Clough, T. J. (2018). Nitrous oxide emissions and biogeochemical responses to soil freezing-thawing and drying-wetting. *Soil Biology and Biochemistry*, 117, 5–15. <https://doi.org/10.1016/j.soilbio.2017.10.040>
- Davis, K. J., Obland, M. D., Lin, B., Lauvaux, T., O'Dell, C., Meadows, B., et al. (2018). ACT-America: L3 merged in situ atmospheric Trace gases and flask data, Eastern USA. ORNL DAAC. <https://doi.org/10.3334/ORNLDAAC/1593>
- de Klein, C., Novoa, R. S. A., Ogle, S., Smith, K. A., Rochette, P., Wirth, T. C., et al. (2006). Chapter 11: N_2O emissions from managed soil, and CO_2 emissions from lime and urea application. In S. Eggleston, L. Buendia, K. Miwa, T. Ngara, & K. Tanabe (Eds.), *2006 IPCC guidelines for national greenhouse gas inventories, Volume 4: Agriculture, forestry and other land use*. IGES.

- Del Grosso, S., Ogle, S. M., Nevison, C., Gurung, R., Parton, W. J., Wagner-Riddle, C., et al. (2022). A gap in nitrous oxide emissions reporting complicates long term climate mitigation. *Proceedings of the National Academy of Sciences*, 119(31), e2200354119. <https://doi.org/10.1073/pnas.2200354119>
- Draxler, R. R., & Hess, G. D. (1998). An overview of the HYSPLIT_4 modeling system of trajectories, dispersion, and deposition. *Australian Meteorological Magazine*, 47, 295–308.
- Eckl, M., Roiger, A., Kostinek, J., Fiehn, A., Huntrieser, H., Knot, C., et al. (2021). Quantifying nitrous oxide emissions in the U.S. Midwest: A top-down study using high resolution airborne in-situ observations. *Geophysical Research Letters*, 48(5), e2020GL091266. <https://doi.org/10.1029/2020GL091266>
- EDGAR4.3.2. (2017). *Emissions database for global atmospheric research, version 4.3.2*. European Commission. <https://doi.org/10.2904/JRC-DATASET-EDGAR>
- EDGAR5.0. (2019). *Emissions database for global atmospheric research, version 5.0*. European Commission.
- Glenn, A. J., Tenuta, M., Amiro, B. D., Maas, S. E., & Wagner-Riddle, C. (2012). Nitrous oxide emissions from an annual crop rotation on poorly drained soil on the Canadian Prairies. *Agricultural and Forest Meteorology*, 166–167, 41–49. <https://doi.org/10.1016/j.agrformet.2012.06.015>
- Hall, B. D., Dutton, G. S., & Elkins, J. W. (2007). The NOAA nitrous oxide standard scale for atmospheric observations. *Journal of Geophysical Research*, 112(D9), D09305. <https://doi.org/10.1029/2006JD007954>
- Hergoualc'h, K., Akiyama, H., Bernoux, M., Chirinda, N., del Prado, A., Kasimir, Å., et al. (2019). Chapter 11: N₂O emissions from managed soils, and CO₂ emissions from lime and urea applications. In E. Calvo Buendia, K. Tanabe, A. Kranjc, J. Baasansuren, M. Fukuda, S. Ngarize, et al. (Eds.), *2019 refinement to the 2006 IPCC guidelines for national greenhouse gas inventories* (Vol. 4). Intergovernmental Panel on Climate Change.
- Hu, L., Andrews, A. E., Thoning, K. W., Sweeney, C., Miller, J. B., Michalak, A. M., et al. (2019). Enhanced North American carbon uptake associated with El Nino. *Science Advances*, 5(6), eaaw0076. <https://doi.org/10.1126/sciadv.aaw0076>
- Janssens-Maenhout, G., Crippa, M., Guizzardi, D., Muntean, M., Schaaf, E., Dentener, F., et al. (2019). EDGAR v4.3.2 Global Atlas of the three major greenhouse gas emissions for the period 1970–2012. *Earth System Science Data*, 11(3), 959–1002. <https://doi.org/10.5194/essd-11-959-2019>
- King, A. E., Rezanezhad, F., & Wagner-Riddle, C. (2021). Evidence for microbial rather than aggregate origin of substrates fueling freeze-thaw induced N₂O emissions. *Soil Biology and Biochemistry*, 160, 108352. <https://doi.org/10.1016/j.soilbio.2021.108352>
- Kort, E. A., Eluszkiewicz, J., Stephens, B. B., Miller, J. B., Gerbig, C., Nehrkorn, T., et al. (2008). Emissions of CH₄ and N₂O over the United States and Canada based on a receptor-oriented modeling framework and COBRA-NA atmospheric observations. *Geophysical Research Letters*, 35(18), L18808. <https://doi.org/10.1029/2008GL034031>
- Lan, X., Dlugokencky, E. J., Mund, J. W., Crotwell, A. M., Crotwell, M. J., Moglia, E., et al. (2022). Atmospheric nitrous oxide dry air mole fractions from the NOAA GML carbon cycle cooperative global air sampling network [Dataset]. 1997–2021, Version: 2022-11-21 <https://doi.org/10.15138/53g1-x417>
- Levis, S., Bonan, G. B., Kluzek, E., Thornton, P. E., Jones, A., Sacks, W. J., & Kucharik, C. J. (2012). Interactive crop management in the Community Earth System Model (CESM1): Seasonal influences on land-atmosphere fluxes. *Journal of Climate*, 25, 4839–4859. <https://doi.org/10.1175/JCLI-D-11-00446.1>
- Liang, Q., Nevison, C., Dlugokencky, E., Hall, B. D., & Dutton, G. (2022). 3-D atmospheric modeling of the global budget of N₂O and its isotopologues for 1980–2019: The impact of anthropogenic emissions. *Global Biogeochemical Cycles*, 36(7), e2021GB007202. <https://doi.org/10.1029/2021GB007202>
- Lin, J. C., Gerbig, C., Wofsy, S. C., Andrews, A. E., Daube, B. C., Davis, K. J., & Grainger, C. A. (2003). A near-field tool for simulating the upstream influence of atmospheric observations: The Stochastic Time-Inverted Lagrangian Transport (STILT) model. *Journal of Geophysical Research*, 108(D16), 4493. <https://doi.org/10.1029/2002JD003161>
- Lu, C., Yu, Z., Zhang, J., Cao, P., Tian, H., & Nevison, C. (2022). Century-long changes and drivers of soil nitrous oxide (N₂O) emissions across the contiguous United States. *Global Change Biology*, 28(7), 2505–2524. <https://doi.org/10.1111/gcb.16061>
- McKain, K., Sweeney, C., Baier, B., Crotwell, A., Crotwell, M., Handley, P., et al. (2022). NOAA global greenhouse gas reference network flask-air PFP sample measurements of CO₂, CH₄, CO, N₂O, H₂, SF₆ and isotopic ratios collected from aircraft vertical profiles [Dataset]. Version: 2022-12-01. <https://doi.org/10.15138/39HR-9N34>
- Mesinger, F., DiMego, G., Kalnay, E., Mitchell, K., Shafran, P. C., Ebisuzaki, W., et al. (2006). North American regional Reanalysis. *Bulletin of the American Meteorological Society*, 87(3), 343–360. <https://doi.org/10.1175/bams-87-3-343>
- Miller, S. M., Kort, E. A., Hirsch, A. I., Dlugokencky, E. J., Andrews, A. E., Xu, X., et al. (2012). Regional sources of nitrous oxide over the United States: Seasonal variation and spatial distribution. *Journal of Geophysical Research*, 117(D6), D06310. <https://doi.org/10.1029/2011jd016951>
- National Centers for Environmental Prediction/National Weather Service/NOAA/U.S. Department of Commerce. (2005). *NCEP North American Regional Reanalysis (NARR)*. Research Data Archive at the National Center for Atmospheric Research, Computational and Information Systems Laboratory. Retrieved from <http://rda.ucar.edu/datasets/ds608.0/>
- NCCOS (National Centers for Coastal Ocean Science)/NOAA/U.S. Department of Commerce. (2022). NOAA ensemble hypoxia forecast. Retrieved from https://cdn.coastalscience.noaa.gov/page-attachments/news/2022_Hypoxia_OnePager.pdf
- Nehrkorn, T., Eluszkiewicz, J., Wofsy, S., Lin, J., Gerbig, C., Longo, M., & Freitas, S. (2010). Coupled weather research and forecasting-stochastic time-inverted Lagrangian transport (WRF-STILT) model. *Meteorology and Atmospheric Physics*, 107(1–2), 51–64. <https://doi.org/10.1007/s00703-010-0068-x>
- Nevison, C., Andrews, A., Thoning, K., Dlugokencky, E., Sweeney, C., Miller, S., et al. (2018). Nitrous oxide emissions estimated with the CarbonTracker-Lagrangian North American regional inversion framework. *Global Biogeochemical Cycles*, 32, 463–485. <https://doi.org/10.1002/2017GB005759>
- Nishina, K., Ito, A., Hanasaki, N., & Hayashi, S. (2017). Reconstruction of spatially detailed global map of NH₄⁺ and NO₃⁻ application in synthetic nitrogen fertilizer. *Earth System Science Data*, 9(1), 149–162. <https://doi.org/10.5194/essd-9-149-2017>
- Nowatzke, L., & Arbuckle, J. G., Jr. (2016). *Iowa Farmers and the Iowa nutrient reduction strategy: 2015 survey results*. SOC 3078 (p. 16). Department of Sociology, Iowa State University.
- Ramankutty, N., & Foley, J. A. (1998). Characterizing patterns of global land use: An analysis of global croplands data. *Global Biogeochemical Cycles*, 12, 667–685.
- Ravishankara, A., Daniel, J., & Portmann, R. (2009). The dominant ozone-depleting substance emitted in the 21st century. *Science*, 326(5949), 123–125. <https://doi.org/10.1126/science.1176985>
- Saikawa, E., Prinn, R. G., Dlugokencky, E., Ishijima, K., Dutton, G. S., Hall, B. D., et al. (2014). Global and regional emissions estimates for N₂O. *Atmospheric Chemistry and Physics*, 14(9), 4617–4641. <https://doi.org/10.5194/acp-14-4617-2014>

- Stein, A. F., Draxler, R. R., Rolph, G. D., Stunder, B. J. B., Cohen, M. D., & Ngan, F. (2015). NOAA's HYSPLIT atmospheric transport and dispersion modeling system. *Bulletin of the American Meteorological Society*, 96(12), 2059–2077. <https://doi.org/10.1175/BAMS-D-14-00110.1>
- Sweeney, C., Karion, A., Wolter, S., Newberger, T., Guenther, D., Higgs, J. A., et al. (2015). Seasonal climatology of CO₂ across North America from aircraft measurements in the NOAA/ESRL global greenhouse gas reference network. *Journal of Geophysical Research: Atmospheres*, 120(10), 5155–5190. <https://doi.org/10.1002/2014JD022591>
- Tenuta, M., Gao, X., Flaten, D., & Amiro, B. (2016). Lower nitrous oxide emissions from anhydrous ammonia application prior to soil freezing in late fall than spring pre-plant application. *Journal of Environmental Quality*, 45(4), 1133–1143. <https://doi.org/10.2134/jeq2015.03.0159>
- Tenuta, M., Gao, X., Flaten, D., Amiro, B., & Gervais, M. (2019). Lower nitrous oxide emissions from anhydrous ammonia application prior to soil freezing in late fall than spring pre-plant application. *Agricultural and Forest Meteorology*, 276–277, 107636. <https://doi.org/10.1016/j.agrformet.2019.107636>
- Thompson, R. L., Lassaletta, L., Patra, P. K., Wilson, C., Wells, K. C., Gressent, A., et al. (2019). Acceleration of global N₂O emissions seen from two decades of atmospheric inversion. *Nature Climate Change*, 9(12), 993–998. <https://doi.org/10.1038/s41558-019-0613-7>
- Thoning, K., Hu, L., Andrews, A. E., Sweeney, C., Miller, J. B., Michalak, A. M., et al. (2019). GMD CT-Lagrange inversions [Software]. National Oceanic and Atmospheric Administration. Retrieved from <https://gml.noaa.gov/ccgg/carbontracker-lagrange/doc>
- USEPA. (2021). *Inventory of greenhouse gas emissions and sinks: 1990–2019*. United States Environmental Protection Agency, EPA 430-R-21-005.
- Wagner-Riddle, C., Congreves, K. A., Abalos, D., Berg, A. A., Brown, S. E., Ambadan, J. T., et al. (2017). Globally important nitrous oxide emissions from croplands induced by freeze–thaw cycles. *Nature Geoscience*, 10(4), 279–283. <https://doi.org/10.1038/Ngeo2907>
- Wei, Y., Shrestha, R., Pal, S., Gerken, T., Feng, S., McNelis, J., et al. (2021). Atmospheric carbon and transport—America (ACT-America) datasets: Description, management, and delivery. *Earth and Space Science*, 8(7), e2020EA001634. <https://doi.org/10.1029/2020EA001634>
- Yadav, V., & Michalak, A. M. (2013). Improving computational efficiency in large linear inverse problems. *Geoscientific Model Development*, 6(3), 583–590. <https://doi.org/10.5194/gmd-6-583-2013>